Chemical Engineering Science 134 (2015) 399–413

Contents lists available at ScienceDirect

Chemical Engineering Science

journal homepage: www.elsevier.com/locate/ces

Influence of wall friction on flow regimes and scale-up of counter-current swirl spray dryers

Victor Francia [a,b,*], Luis Martin [b], Andrew E. Bayly [b,1], Mark J.H. Simmons [a]

[a] School of Chemical Engineering, University of Birmingham, Birmingham, United Kingdom
[b] Procter & Gamble R&D, Newcastle Innovation Centre, Newcastle upon Tyne, United Kingdom

HIGHLIGHTS

- We study the vortex flow in swirl dryers across full scale designs and conditions.
- Three air flow regimes are related to the effects of friction and design features.
- The characteristics of deposits are vital to explain the evolution of the vortex.
- Friction reduces the swirl drastically and it has a major impact on the turbulence.
- Flow regime prediction facilitates the use of new control and scale-up criteria.

ARTICLE INFO

Article history:
Received 1 December 2014
Received in revised form
25 March 2015
Accepted 23 April 2015
Available online 2 May 2015

Keywords:
Spray drying
Vortex flow
Scale up
Roughness
Recirculation
Swirl decay

ABSTRACT

The structure of the vortex flow in swirl spray dryers is investigated after having fouled the walls with deposits typical of detergent manufacture. The range of *Re* and swirl intensity Ω characteristic of industry are studied using three counter-current units of varying scale and design. The friction with the deposits increases the flow turbulence kinetic energy and causes a drastic attenuation of the swirl and as a result, the vortex breaks down in the chamber forming recirculation regions (i.e. areas of reverse flow). Three flow regimes (1) no recirculation, (2) central and (3) annular recirculation have been identified depending on the swirl intensity. New control and scale up strategies are proposed for swirl dryers based in predicting the decay and the flow regime using the unit geometry (i.e. initial swirl intensity Ω_i) and experimental decay rates function of the coverage and thickness of deposits. The impact in design and numerical modelling must be stressed. Adequate prediction of the swirl is vital to study fouling and recirculation, which surely play an important part in the dispersion and aggregation of the solid phase. Current models have no means to replicate these phenomena, and yet, in this case neglecting the deposits and assuming smooth walls would result in (a) over-prediction of swirl velocity up to 40 – 186% (b) under-prediction of turbulent kinetic energy up to 67 – 85% and (c) failure to recognise recirculation areas.

1. Introduction

Spray drying serves many industries for the generation of particulate products. Co-current dryers are used for production of temperature degradable powders such as food, pharmaceuticals or enzymes, and are the main focus of research into fluid dynamics, wall deposition and inter-particle interactions in spray drying systems (e.g. Verdurmen et al., 2004). Research into counter-current towers is much more limited; being larger in volume, there are very few data at full scale. They are used in the manufacture of thermally stable products such as detergents, and in some cases make use of a strong swirling flow, which entails a more complex fluid dynamics but improves the heat and mass transfer efficiency. Swirl is introduced in many other devices with the same objective but at much smaller scale. It is in this context, for instance in open tubes with tangential inlets (e.g. Chang and Dhir, 1994, 1995), or pipes where most of the studies of decaying swirling flows have focused (e.g. Kitoh, 1991; Steenbergen and Voskamp, 1998). In larger devices such as centrifugal separators, frictional losses (Kaya et al., 2011) and the solids loading are also known to attenuate the swirl (e.g. Hreiz et al., 2011) and affect the collection efficiency in a

* Corresponding author at: School of Chemical Engineering, University of Birmingham, Birmingham, United Kingdom.
E-mail address: v.francia.chemeng@gmail.com (V. Francia).
[1] Present address: School Chemical and Process Engineering, University of Leeds, Leeds, United Kingdom.

http://dx.doi.org/10.1016/j.ces.2015.04.039

range of designs (e.g. Hoffmann et al., 1992; Kim and Lee, 2001; Cortes and Gil, 2007; Chen and Shi, 2007).

On the other hand, the stability of turbulent swirling flows is a very wide subject, characteristic of confined units such as combustors where the intensity of the swirl is higher. The confinement and the centrifugal effects give rise to instabilities and result in drastic changes in the structure referred to as a vortex breakdown (*VBD*), documented as function of the Reynolds, *Re*, number and the circulation (Luca-Negro and O'Doherty, 2001). The breakdown can manifest in the form of periodical structures as the precession of the vortex core (*PVC*) (Syred, 2006) and produce recirculation regions depending on the effect of the downstream boundaries (Luca-Negro and O'Doherty, 2001) particularly when the flow faces a restrictive exit contraction (Escudier et al., 1980; Derksen, 2005). Similar instabilities occur in cyclones where many authors have examined the flow structure and turbulence fields (e.g. Hoekstra et al., 1999; Liu et al., 2006). In particular, reverse-flow designs provide clear evidence of the consequences of swirl attenuation. The vortex can break down within the outlet exit (Derksen and Van den Akker, 2000), and in occasions the decay of the swirl gives rise to the "end of vortex" phenomenon (Peng et al., 2005; Pisarev et al., 2011) whereby the core deviates from the centreline of the chamber and attaches to the wall, with a serious detriment in performance. The end of vortex then leads to the concept of "natural length" of cyclones used in design to prevent the destabilization (Hoffmann et al., 1995; Cortes and Gil, 2007; Avci et al., 2013). Swirl dryers present a similar set up, but in a once-through flow whereby the vortex reaches a contraction at high swirl velocities. The work in dryers however is much more limited because gathering measurements in full scale (i.e. volume $>100-1000\ m^3$) is a serious practical challenge. Visualisation studies were common to describe counter-current units (e.g. Paris et al., 1971; Sharma, 1990) but detailed air velocity data have only been obtained in laboratory (Bayly et al., 2004) or pilot scale facilities where laser based methods are more easily applied (Zbicinski and Piatkowski, 2009). The quantity and level of detail is much more restricted in full scale, and limited to small sections (Hassall, 2011; Wawrzyniak et al., 2012). Yet, it is vital to study the flow in production units because only they can replicate characteristics such as: (a) the presence of deposits at the walls (b) the range of designs of the cone, the air distributor to the inlets or the exhaust lines and b) the range of *Re* and swirl intensity, Ω.

In our previous paper (Francia et al., 2015a) we investigated the structure, turbulence and stability of the vortex in a swirl spray dryer after having cleaned the walls. In these conditions the swirl intensity, Ω, decays further than anticipated in the past, which is linked to the large wall roughness characteristic of production dryers even after having cleaned the walls mechanically. The data in a cleaned full scale tower explained the origin of historical discrepancies between velocities in dryers with smooth walls (Bayly et al., 2004) or numerical simulations, and the few reports in large dryers (Hassall, 2011).

In this paper, we explore the influence of the presence of actual wall deposits in production units and how they must be considered in control and scale up. The scenario in Hassall (2011) or Francia et al. (2015a) provides a useful base to understand the flow behaviour and advance in numerical modelling (Ali, 2014), but it is still far from the real system as accounts not for (a) actual wall conditions, since deposits are known to grow very thick as bands and patches of wet powder, or (b) the range of designs and scales of swirl tall-form dryers, which changes substantially across for instance the detergent industry (Huntington, 2004). Clearly, the question of how friction responds to the relevant production conditions is open. This paper addresses some of these questions gathering air velocity and turbulence measurements in three industrial dryers having fouled the walls with deposits characteristic of detergent manufacture. The units are selected to cover the actual range of geometries typical of industry and the operational ranges of swirl intensity Ω and *Re*, including the tower studied in Francia et al. (2015a) for a direct comparison with data under cleaned walls. This study permits one to correlate the swirl decay to the coverage, distribution and thickness of the deposits, and identify three flow regimes dependent on Ω. General standardisation and scale up criteria are then proposed based in the control of the inlet swirl intensity and the use of the equations and rates provided to predict the attenuation of the swirl, and subsequently the recirculation in the dryer.

2. Experimental methodology

2.1. Design, generation of the swirling flow and scale up of counter-current swirl dryers

Three full scale counter current swirl spray drying towers, denoted Scales I, II and III, property of Procter & Gamble Co. have been investigated. Fig. 1 illustrates the design, nomenclature, position of measurements and the design of the inlet ports, and Table 1 summarises the operational conditions and the main aspect ratios. Air velocity measurements have been taken in isothermal conditions and in the absence of particles, by adjusting the relative head of the inlet and exhaust air fans manually in order to obtain a stable target mass rate and exit pressure.

The generation of the vortex is consequent upon the orientation of the inlets and the design of the hip and the cone sections at the bottom of the dryer. An open bustle ring is used as the air distributor, denoted plenum in Fig. 1. It feeds the air into a series of ports that are arranged symmetrically at the bottom of the cylinder. The inlet ports inject the air flow towards the conical section with a certain angular momentum given by the alignment angles, φ and ξ, to the radial axis and the horizontal plane respectively (see Fig. 1b). The swirling motion generated causes the formation of a vortex that rises into the cylinder until converging inwards and exiting through a central duct at the top, denoted vortex finder. The exit presents a series of internal channels named straighteners, which break the swirl before the air is directed into cyclone separators. The strength of the swirling motion is quantified by the use of a circulation parameter, or swirl intensity, Ω. Section 3 defines Ω in the chamber as the non-dimensional flux of angular momentum, G_θ, normalised by an average axial momentum, $G_{z,av}$, based upon the superficial air velocity, $\overline{U}_{av}$. On the same basis, an initial geometrical value denoted Ω_i can be defined Eq. (1) as a characteristic design parameter (Francia et al., 2015a)

$$\Omega_i = \frac{G_{\theta,i}}{R\cdot G_{z,av}} = \frac{\overline{M}_i \overline{U}_{i,\theta} R_i/\pi R^2}{\overline{M}_C \overline{U}_{av} R/\pi R^2} = \frac{\overline{M}_i^2}{\overline{M}_C^2}\frac{A_C}{A_i}\frac{R_i}{R}\cdot \sin\varphi\cos\xi \quad (1)$$

function of the inlet alignment(s), the ratio between the mass rate through the inlets $\overline{M}_i$ and the cylinder $\overline{M}_C$ (i.e. owed to air entrainment from the bottom end, $<5\%$ of $\overline{M}_C$) and ratios specific to the tower design, between the cylinder radius R_C and the radius at the inlet R_i ring, and between the combined area of the inlets, A_i and the cylinder, A_C.

Scaling spray dryers is a very complex task. The work of Oakley (1994, 2004) describes salient dimensionless numbers and the difficulty in scaling the flow of the solids. A co-current dryer achieves dynamic similarity in low or high *Re* numbers (associated to entrained particles or high velocity drops) through scaling the ratio of the droplet sizes with the square or the ratio of the chamber diameters, somewhere in between the design values for chambers with centrifugal atomizers ~ 1.5. Oakley (1994) recognises these criteria are valid for particles unaffected by gravity. Otherwise patterns are difficult to scale, (e.g. big chambers or large

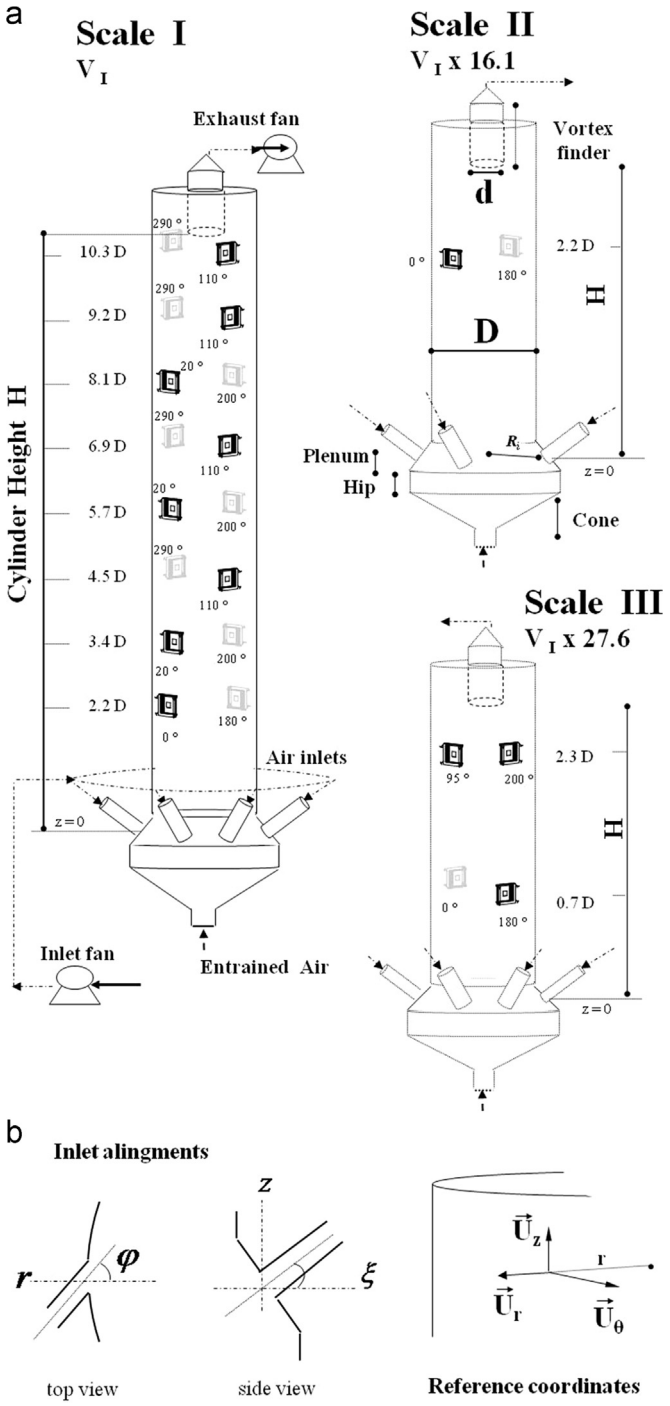

Fig. 1. (a) Nomenclature, design, air delivery system and location of accesses. Volume relative to Scale I. (b) Detail of an air inlet port: alignments φ and ξ, and reference coordinates.

particle sizes) and from the use of computational fluid dynamic models becomes a key (Oakley, 2004). This is particularly true in counter-current units where gravity is essential to drive the sedimentation of solids. Indeed the product varies from entrained fines to large particles insensitive to turbulence and contains certain size fractions that tend to accumulate. In swirl assisted units the dispersion of the solids is further complicated by the migration to the walls. Scale up dimensionless numbers are available for centrifugal separators based in geometrical ratios, *Re* and a Stokes number to describe the solids motion (e.g. Butner, 1999; Zhao, 2010). The Froude number, which evaluates the influence of gravity, can be often neglected and the analysis

Table 1
Summary of the tower geometry, total volume, V, initial swirl intensity, Ω_i, superficial air velocity, $\overline{U}_{av} = \overline{M}_C/\overline{\rho}.A_C$, and Reynolds number, $Re = \overline{\rho}.D.\overline{U}_{av}/\overline{\mu}$

Design		*Scale I*	*Scale II*	*Scale III*
H/D		10.58	2.97	2.87
d/D		0.29	0.28	0.31
R_i/R		$r_{c,1}$	$r_{c,2} < r_{c,1}$	$r_{c,2} < r_{c,1}$
Ω_i		5.1–5.4	3.4–3.6	7.7–8.2
$V/V_{\text{Scale I}}$		1.0	16.1	27.6
Operation			$Re \cdot 10^{-5}$	$\overline{U}_{av}/\overline{U}_{av,Re_1}$
	Re_1		1.04–1.09	0.98–1.02
Scale I	Re_2		1.47–1.50	1.39–1.44
	Re_3		2.21–2.24	2.09–2.17
Scale II	Re_4		6.74–6.91	1.81–1.85
Scale III	Re_5		4.79–5.12	1.04–1.10

pursues to describe the tendency of the solids to reach the walls and be collected. This logic is only partially applicable in counter-current dryers where particles indeed move outwards, but in this case it is precisely the counter air flow and gravity which determine the sedimentation. In addition, dryers also show extensive agglomeration, which disrupts significantly the Stokes number and the cyclone efficiency (Paiva et al., 2010).

In reality, powder of a similar size is manufactured in swirl towers of different scale, which requires engineers to have some way of controlling the residence time of the solids in the chamber. Large units tend to maintain roughly similar ranges of air superficial velocities and thus particle sedimentation velocities, and so engineers control the particle residence time τ_p by adjusting the length of the cylinder (i.e. H/D) and the position of the atomizers. In essence, this means that while *Re* increases with increasing scale ($\propto D$), the centrifugal inertia of the solids diminishes ($\propto D^{-1}$); hence, the lack of dynamic similarity. Balancing both effects is major challenge when scaling dryers: that is (a) control the action of gravity, which can be characterised by a residence time given by the ratio of the sedimentation velocity and the position of atomizers (i.e. particle accumulation, drying and agglomeration) and (b) the centrifugal inertia, which similarly to a cyclone, it could be described by a stokes number (i.e. a preferential concentration near the wall and fouling).

This paper is limited only to study of the air flow phase and how this can be used to control desired effects in the dispersion of the solids. It concerns with the effect that the design and the deposits have in the dynamics of the air flow and how the attenuation of the swirl must be accounted for. The towers used operate at a different initial swirl intensity Ω_i. The radius of the plenum and the area of the inlet ports (i.e. R_i/R and A_C/A_i in Eq. (1)) are modified so that the units denoted Scale II and III operate at a common R_i/R and at lower and higher Ω_i than Scale I respectively. For the sake of simplicity, other parameters and design features known to impact the vortex development are kept constant: a) the contraction ratio d/D, which plays an important role in the stabilisation of the flow in combustors (Escudier et al., 1980; Escudier and Keller, 1985) and b) the inlet alignment φ and ξ, and the design of the hip and cone discussed by Huntington (2004) which according to Sharma (1990) and later Harvie et al. (2001) can disrupt significantly the shape, stability and symmetry of the flow.

2.2. Particulate wall deposits and roughness height

Deposits do not form in a tower in a homogeneous manner, but develop as bands on the wall. Their characteristics vary according to the position of slurry atomizer(s) and the drying conditions. Bottom sections of deposit show a highly compacted structure,

being subject to faster drying and stronger aerodynamic stresses. In contrast, at the top, the deposits show lower densities and a high moisture because they are formed by elutriated droplets, face weaker stresses and do not dry, under the cooler local conditions. The thickest bands appear in the proximity of the slurry atomizer (s). Here, a fraction of the atomised droplets projects onto the wall at a high momentum and builds up thick multi-layered structures (Hassall, 2011). Three different deposits configurations have been investigated in Scale I, namely Case A, B and C:

- *A: Cleaned walls.* Conditions associated to unit start up before production begins, reported in Francia et al. (2015a)
- *B: Standard operation.* Conditions associated with short term production (i.e. a single cycle in steady state) where the walls have been previously cleaned. They correspond to the fouling study available in Francia et al. (2015b).
- *C: Heavy deposition.* Conditions associated to a series of long term productions (i.e. multiple start-up and production cycles) with either partial or no intermediate automatic cleaning.

Figs. 2 and 3 show the resulting distribution of deposits, and their typical structure. Measurement of the coverage and the thickness are summarised in Table 2 with rough estimates obtained from analysis of photographs and measurements at the inspection hatches shown in Fig. 1. Nonetheless, they allow one to define the length scale of the bands or patches in different sections and compare them with the development of the flow field.

The thickness, δ/D shown in Table 2 is above the maximum non-dimensional roughness height, ε/D, reported in pipes. Only in Case A can the entire wall be considered homogeneous and

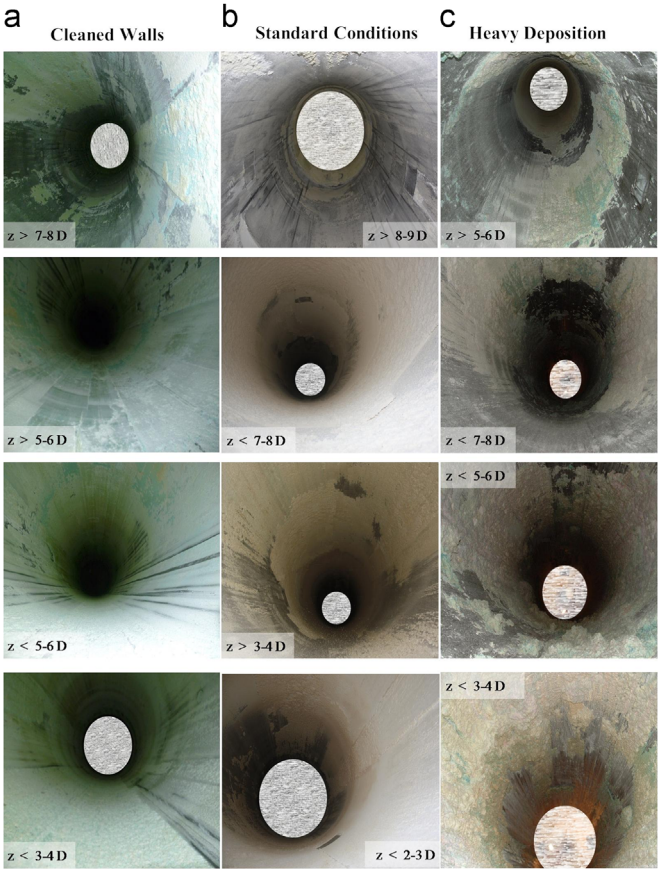

Fig. 2. Visual inspection of deposits in Case A (a), Case B (b) and Case C (c). Each photograph shows the section of the cylinder noted. Nozzle(s) and/or internal instrumentation have been artificially removed to protect intellectual property.

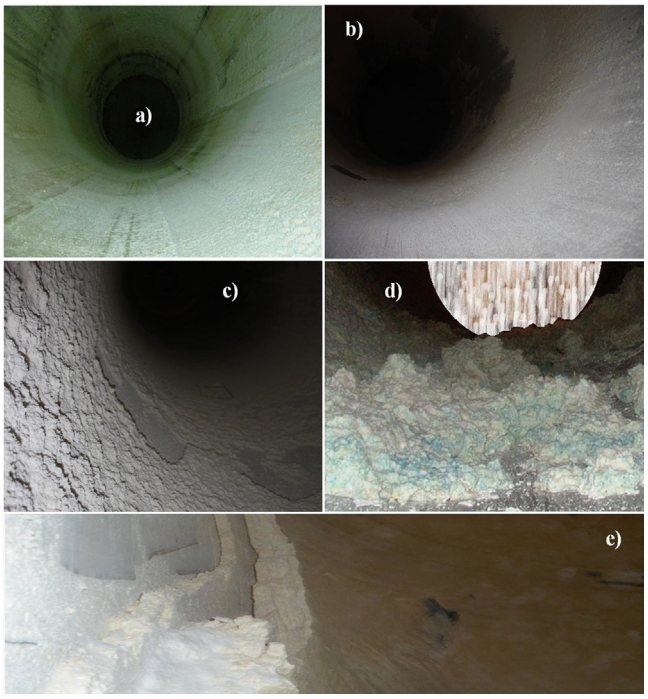

Fig. 3. Detail of the morphology of the deposits. Bottom section of the chamber in Cases A (a) and B (b). Spray region in Cases B (c) and C (d) and a transversal cut in Scale III (e) showing a large thickness but homogeneous roughness.

Table 2
Axial distribution of deposits. The range of thickness and coverage of the wall for different sections covered either by patches (< 100%) or a full band (100%). The section including the projection of the atomizer given in bold.

	Section z/D		***Coverage*** % **in** θ		***Thickness*** $10^2 \cdot \delta/D$	
	From	To	From	To	From	To
Case A	Cone		100		< 0.6	
	0.0	7.1				
	7.1	10.6	0	40	0	< 0.6
Case B	Cone		100		< 0.6	
	0.0	1.8	15	30	0	< 0.6
	1.8	2.4	100		< 0.6	
	2.4	5.7	40	70	0	< 0.6
	5.7	**7.1**	**100**		**0.6**	**1.2**
	7.1	8.1			0	0.6
	8.2	10.6	Metal		Metal	
Case C	Cone		Metal		Metal	
	0.0	2.4	5	10	0	< 1.2
	2.4	**5.7**	**50**	**75**	**0.6–1.2**	**1.8–3.0**
	5.7	7.1	10	15		
	7.1	8.1	100		0	< 1.2
	8.1	10.6				< 0.6

the range of variation of δ/D may related to ε/D and comparable to a fully rough flow (Francia et al., 2015a). In Cases B and C, the ε/D within a single band or patch of deposits is much lower than its thickness δ/D, but in turn it presents a complex two dimensional nature. The multi-layer structure of the deposits has elements of a wide range of sizes. They come from the voids left behind by the erosion of small particles (i.e. $100-1000\ \mu m$) up to the detachment of pieces of several centimetres, which leave cavities of a very large length but with a depth limited by δ/D. This occurs in sections where the multi-layer extends homogenously (i.e. within the bands given in Table 2, and across the entire surface in Scales II and III). In contrast, at the edges of

bands, or between the patches, the abrupt change in the thickness represents an obstacle to the flow (see Fig. 2). In these sections, the variation in δ/D given in Table 2 is perhaps a better indication of the drag originated.

2.3. Instrumentation

Velocity data were collected with a Horizontal Symmetry 50 Solent Sonic Anemometer (Gill Instruments Ltd.). It comprises of a single metal frame and three pairs of ultrasonic transducers, which serve to compute the air velocity in three independent directions in a finite volume with a temporal resolution of 50 Hz. Previous works provide a more detailed discussion on the corrections and the methodology to apply sonic anemometers to large dryers or cyclones, the restrictions to be considered and conservative ranges of the uncertainty (Francia, 2015; Francia et al., 2015c). The instrument is placed at a given position by fixing it to a unit door engineered to be assembled around the anemometer frame and sliding the head containing the transducers into the dryer. The accuracy in wind tunnel calibration is reported as 1% *RMS* in velocity magnitude and 1° in direction, but in the context described here, errors increase to $<1-4$ % velocity magnitude and $<3°$ in direction, and $7-31$ % in the turbulent kinetic energy, κ. The uncertainty is mainly due to the disruption caused by the instrument, but includes errors arising from the method, short-comings assumptions in the working principle of commercial instruments and long time scale variability in large units. The reproducibility of the measurements has been found within the ranges given above as long as the conditions of the walls are unchanged.

3. Analysis

Measurements are taken for 60 s at a reporting frequency of 50 Hz with the exception of Case C, at 20 Hz. The normal and Reynolds stresses are derived from the statistics of the velocity signal and the Reynolds decomposition. Integral parameters such as the swirl intensity Ω are computed according to the definition of Kitoh (1991) discussed below. A Fast Fourier Transform is used to identify periodic signals in the velocity associated not to a turbulent origin but indicative of periodic flow structures.

Sloan et al. (1986) or Weber and Dugué (1992) describe the computation of swirl numbers from an angular momentum balance and strict definitions including pressure and turbulent terms. As in other decaying swirling flows, these are too complex for the use in swirl tubes or dryers, which can be more easily characterised by the swirl intensity given by Kitoh (1991) in Eq. (2). Ω is defined as the non-dimensional flux of angular momentum neglecting the contribution of the Reynolds stress and the axial flow development (Steenbergen and Voskamp, 1998) and normalised by the axial flux of momentum based in the superficial velocity, $\overline{U}_{av}$, and the tower radius, R.

$$\Omega = 2\pi\rho \int_0^R \frac{\overline{U}_z \overline{U}_\theta}{\rho\pi \overline{U}_{av}^2 R^3} r^2 . dr \tag{2}$$

The relation between Ω and the non-dimensional tangential wall shear stress, $\tau_{w,\theta}$ in Eq. (3) can be obtained from the Reynolds averaged equations assuming symmetry, stationary flow and incompressibility (Steenbergen and Voskamp, 1998; Najafi et al., 2011). The usual expressions for the exponential decay of Ω reported in literature are quoted in Eqs. (4) and (5), derived assuming $\tau_{w,\theta}$ and Ω are proportional (Steenbergen and Voskamp, 1998; Najafi et al., 2011) or follow a piecewise relation in the range of study (Senoo and Nagata, 1972; Kitoh, 1991).

$$\frac{2\tau_{w,\theta}}{\frac{1}{2}\rho \overline{U}_{av}^2} = \frac{d\Omega}{d(z/D)} \tag{3}$$

$$\Omega = \Omega_{ref} \cdot e^{-\lambda\left(\frac{z-z_{ref}}{D}\right)} \tag{4}$$

$$\Omega = \left(\Omega_{ref} + \frac{B}{A}\right) \cdot e^{2A\left(\frac{z-z_{ref}}{D}\right)} - \frac{B}{A} \tag{5}$$

Eq. (4) holds in open pipes only for very small Ω values but in regions above the Eq. (5) must be used where Ω_{ref} and z_{ref} define an initial reference point. Similarly to our previous work (Francia et al., 2015a) several estimates of Ω are computed to illustrate the scale of the errors. Measurements are not available in the near wall region and the centre of the cylinder in Scales II and III, and so extrapolation is required. The best estimate, Ω_o, considers that (a) at the centre $\overline{U}_\theta$ reaches zero and $\overline{U}_z$ takes the value of the closest measurement (i.e. a jet-like profile) and (b) near the wall the $\overline{U}_\theta$ and $\overline{U}_z$ are reconstructed by linear extrapolation between the last measurement and an intermediate point after which the velocity follows the logarithmic law of the wall. The boundary layer thickness is estimated so that the integration of $\overline{U}_z$ in the cross section complies with the known volume rate. Under and over predictions are denoted Ω_- and Ω_+, whereby the velocity is reconstructed with a) Ω_-: a linear decrease from the last measurement to zero at the wall or b) Ω_+: a constant value. Ω_- leads much larger errors in the computation of the volume rate since it severely underestimates the logarithmic region in Cases B and C, but errors in Ω_o are kept $<0.1\%$ with the exception of strongly asymmetrical sections (i.e. up to 4% in Scale I or II, or 13% at the top of Scale III).

4. Results and discussion

In our previous paper we reported the velocity and turbulence fields under cleaned walls in Scale I, denoted Case A (Francia et al., 2015a). In this work, selected data are taken as a reference for comparison to the structures observed when the walls are fouled in Cases B and C and at different designs in Scales II and III. Sections 4.1.1 and 4.1.2 describe the effect of increasing friction and how recirculation zones appear. Sections 4.1.3 and 4.1.4 show the effect of the inlet distributor and *Re* in symmetry and Sections 4.1.5 and 4.1.6 report the swirl decay rates and discuss scale up and control. The production of turbulence is shown in Section 4.2.1 and Reynolds stresses and periodicity in Sections 4.2.2 and 4.2.3.

4.1. Time averaged velocity field

4.1.1. Wall friction

Figs. 4 and 5 show the evolution of the tangential $\overline{U}_\theta$ and axial velocity, $\overline{U}_z$, across the cylindrical chamber for the same bulk flow (Re_2 in Table 1) and different deposits in Cases B and C, and compares it with the structure for the same *Re* under clean walls taken from Francia et al. (2015a). Many swirling flows are characterised by the extension of an inner forced-like vortex (i.e. a linear increase in $\overline{U}_\theta$ with r) and an outer free-like vortex (i.e. an inverse relation between $\overline{U}_\theta$ and r) and the transition or annular region that blends both. In Fig. 4 all cases show a similar maximum $\overline{U}_\theta$ value at the bottom of the unit (see Fig. 4a), but the forced vortex developed at the centre in Cases B and C is much wider. As the flow rises, the transfer of angular momentum to the exit shifts $\overline{U}_{\theta,Max}$ towards the centre, and the transition region shows an abrupt change. In Case B, the forced vortex retains a radius

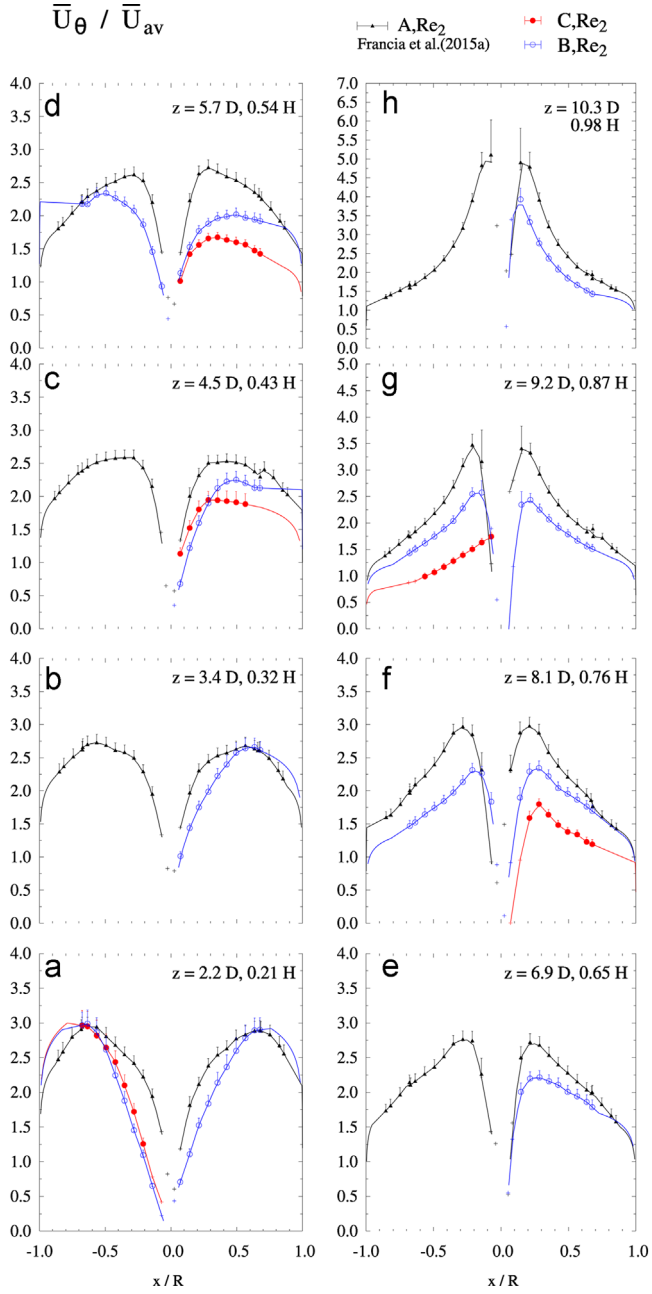

Fig. 4. Scale I. Tangential velocity $\overline{U}_\theta$ in Cases B and C and comparison to data under cleaned walls, Case A, taken from Francia et al. (2015a). Across 1 diameter, $x=-r$ for $\theta<\pi$ and $x=r$ for $\theta>\pi$.

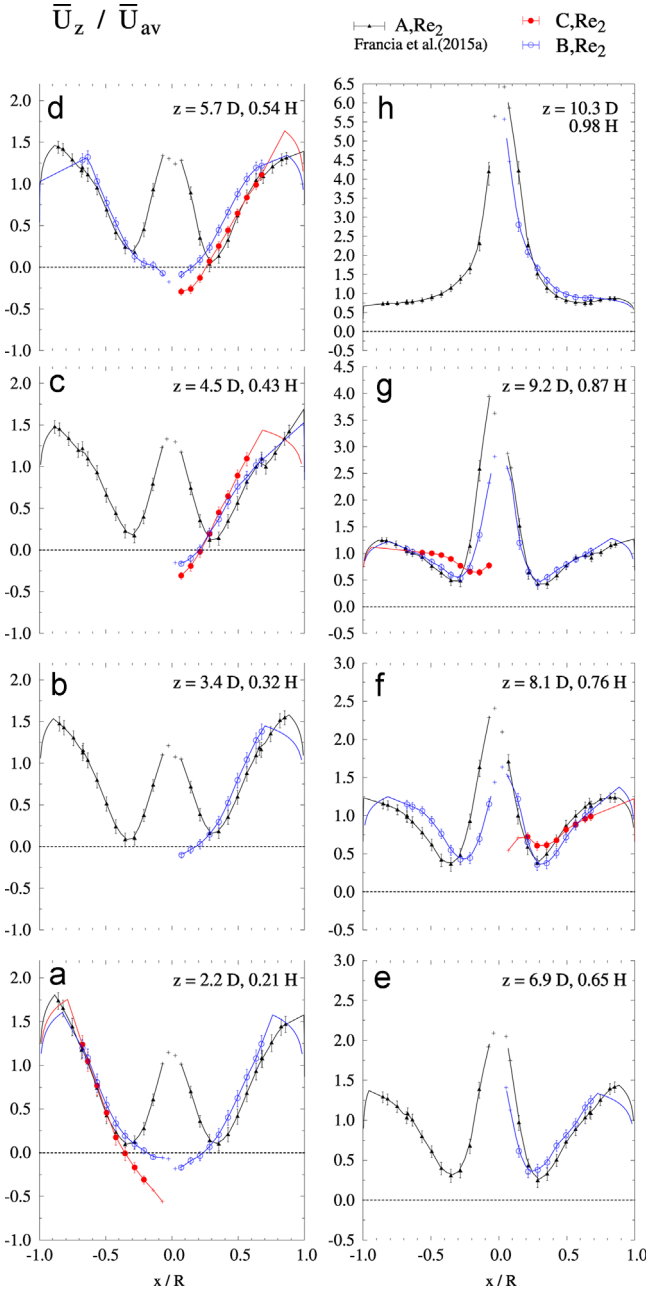

Fig. 5. Scale I. Axial velocity $\overline{U}_z$ in Cases B and C and comparison to data under cleaned walls, Case A taken from Francia et al. (2015a). Across 1 diameter, $x=-r$ for $\theta<\pi$ and $x=r$ for $\theta>\pi$.

$r=0.20-0.30R$ in the levels $z\leq 4.5D$, after which it narrows rapidly to $r<0.10-0.15R$ in $z=6.9\ D$. In Case C, a similar change occurs at a lower position. The radius of the inner forced vortex narrows from $r>0.30-0.40\ R$ at $z=2.2\ D$ to $r<0.10-15\ R$ at $z=5.7D$. Above this point, all cases develop a Rankine pattern with a free vortex in the outer part where $\overline{U}_\theta$ decreases linearly with r, which then turns into an inverse relation at the top, $z=10.3\ D$.

Similar tangential velocities are observed for $z\leq 3.4D$, but a clear reduction in $\overline{U}_\theta$ becomes evident comparing Case A to B and C in all the regions above, where deposits are significant in Cases B and C (see Figs. 2 and 3). The deficit is as high as $15-30\%$ in Case B, and up to $40-50\%$ in Case C. The change in the pressure field has a remarkable impact in the axial flow. As opposed to the jet observed in Fig. 5 when the walls are cleaned, Cases B and C develop a central recirculation zone, *CRZ*, in the bottom half of the cylinder, $z\leq 5.7D$, where the flow is reversed. The recirculation region exhibits a conical shape: the diameter decreasing axially until the flow reverts back between $5.7\ D<z<6.9\ D$ in Case B, leading to the stagnation of the flow and an abrupt change in direction, referred to as a vortex breakdown, *VBD*. Above the breakdown location, Case B does show a jet that increases in magnitude approaching the exit duct, bringing the position of the minimum axial velocity, $\overline{U}_{z,Min}$ slightly outwards from $z=6.9\ D$ to $9.2D$. The lack of cleaning and longer productions in Case C lead to thicker deposits, which widens the *CRZ* and causes a stronger reverse flow up to $\overline{U}_{z,Min}<-1\ \overline{U}_{av}$ at $z=2.2D$. Once the flow reverts back up between $5.7<z<8.1\ D$ the maximum is not generated at the centre, but displaced outwards. It aligns with the centre only nearby the exit duct. The magnitude of $\overline{U}_z$ at the central jet decreases significantly from Case A to B and C.

The observation of the flow reversion is not surprising. It responds to the adverse pressure gradient generated at the core by high swirl velocities. Chang and Dhir (1994) describe the same phenomenon for tangentially injected flows in an open tube with a similar swirl generation mechanism. In the same swirl intensity range Chang and Dhir (1994) report similar $\overline{U}_\theta$ profiles to Cases B and C characterised by a wide forced vortex and flow reversal at the bottom end of the structure.

4.1.2. Vortex breakdown and recirculation zones

Vortex breakdown are common phenomena in swirl tubes, centrifugal separators or combustors. The swirl causes an adverse axial pressure gradient, which may be sufficient to generate the reversion in the axial flow at the central region depending on the balance between angular and axial momentum flows, denoted swirl number. At swirl numbers $S<0.6$ the radial pressure gradients generated are not strong enough and axial and tangential velocities are not coupled (Luca-Negro and O'Doherty, 2001). But as the swirl increases the adverse pressure gradient generated by centrifugal effects cannot be overcome by the kinetic energy of the flow and it becomes stagnated. This causes a disturbance that can evolve in different ways depending on *Re* and the circulation, leading to several types of breakdown patterns, type 1 to 6, asymmetric structures and periodical phenomena reviewed in detail by Luca-Negro and O'Doherty (2001).

Breakdown is also known to occur in more complex geometries such as in the inlet of dryers (Langrish et al., 2004) or the outlet of reverse-flow cyclones resulting in the precession of the core (Derksen and Van den Akker, 2000). In a sense, the "end of vortex" reported in a reverse-flow arrangement (Pisarev et al., 2011, 2012) is a manifestation of the same instability shown in Fig. 5, whereby the attenuation of the swirl below a certain level destabilises the structure. A dryer however shows an upwards flow and a pressure field more conditioned by the contraction. Francia et al. (2015a) discuss in detail the effect of the exit duct and how it is responsible of the jet observed under cleaned walls. The effect of a contraction is similar to that in non-swirling flows, in the sense that it causes acceleration and a rise in pressure. When the vortex faces a contraction at high swirl intensity the top boundary causes a rise in pressure that is transmitted downstream as a shock wave and inhibits the adverse gradient owed to the swirl (Escudier et al., 1980; Escudier and Keller, 1985). The data shown in Fig. 5 shows that, remarkably, when deposits are present at the walls, the influence of the top boundary is not transmitted as far down in the chamber and the instability expected for open systems arises. In this way, one can distinguish regions associated to (a) the inner jet dominated by the low pressure at the exit, and (b) an outer region dominated by the interaction with the wall.

Fig. 6 shows the transition between different flow regimes according to Cases A, B, C and Scales I, II and III. It provides comparison of the velocity fields and highlights the extension of the jet and the recirculation areas (negative axial velocities). A clear evolution is appreciated according to Ω:

4.1.2.1. Dominated by the contraction. No recirculation, $\Omega_e \geq \sim 1$. *Example: Scale I, Case A, $\Omega_{0.21-0.98H} = 2.02-1.03$* (Francia et al., 2015a). *Scale II, $\Omega_{0.76H} = 1.29$* (Fig. 7a). Under cleaned walls, no *CRZ* is observed. The overall increase in pressure caused by the contraction is transmitted down the cylinder and suppresses the reversal of the axial flow (Escudier and Keller, 1985; Francia et al., 2015a), which explains the high velocities in Fig. 4 and why the jet prevails throughout the chamber. Scale II presents a different aspect ratio and a narrower plenum. However, it operates at a lower Ω_i and in this way it maintains a similar Ω values at the top of the tower (see Section 4.1.4). Fig. 7a shows how this translates into very similar velocity fields at the same relative distance to the exit (i.e. z/H) with the exception of a higher velocity at the core.

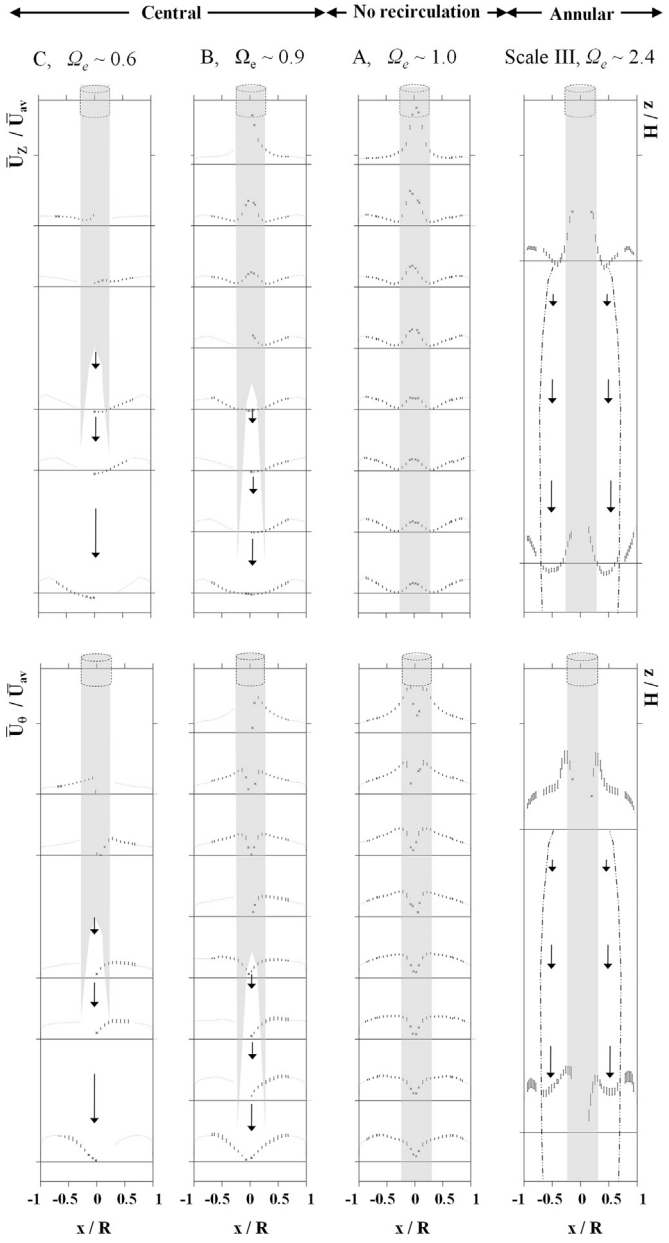

Fig. 6. Flow regimes in counter-current swirl dryers. $d/D \sim 0.30$. Shadowed areas delimit the upwards jet and arrows the areas of reverse flow. Plots to scale of axial velocity $\overline{U}_z$ (top) and tangential velocity $\overline{U}_\theta$ (bottom) for the cylindrical chamber.

4.1.2.2. Dominated by the wall. Central recirculation. $\Omega_e < \sim 1$. *Example: Scale I, Case B, $\Omega_{0.21-0.98H} = 2.11-0.91$* (Figs. 4 and 5). The presence of bands of deposits in Case B increments the friction and reduces $\overline{U}_\theta$ in the upper part. As described in combustor design, the lower swirl intensity nearby the exit makes the influence of the contraction not to extent as far down the cylinder (Escudier et al., 1980; Escudier and Keller, 1985). A wider forced vortex is allowed to form in the bottom section and as a result it generates a *CRZ* of conical shape, in very similar fashion to an open tube (Chang and Dhir, 1994). The diameter of the *CRZ* decreases with axial position and vanishes at a stagnation point where the vortex breaks down splitting the cylinder in two differentiable sections, governed by a) the adverse pressure due to

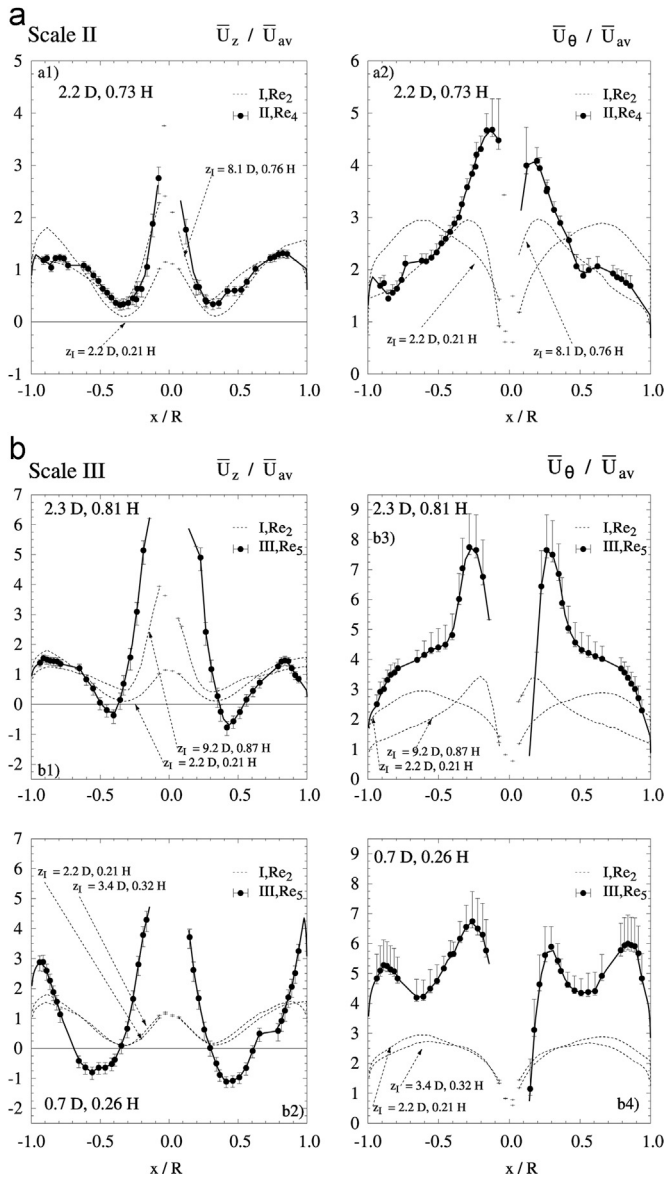

Fig. 7. Velocity field in Scale II and III and comparison to the same axial levels in terms of z/D and z/H under cleaned walls, Case A, from Francia et al. (2015a). (a) Scales II, (b) Scales III. Axial velocity $\overline{U}_z$ (a1, b12) and tangential $\overline{U}_\theta$ (a2, b34).

the swirl at the bottom part or b) the low pressure at the exit duct in the top. In these circumstances, the jet is only generated at regions sufficiently close to the exit.

Example: Scale I, Case C, $\Omega_{0.21-0.98H} = 2.26-0.58$ (Figs. 4, 5 and 9). Prolonged productions and lack of cleaning procedures render more heterogeneous and thicker deposits in Case C, which originates a stronger drag and reduce the swirl further. The vortex then faces the contraction at an even lower Ω and it is easily pulled inwards. The influence upstream of the contraction diminishes, and as a result the *CRZ* widens and extends further up. In this case, the jet-like profile is lost for the most part of the cylinder.

4.1.2.3. Dominated by the contraction. Annular recirculation, $\Omega_e \geq \sim 2.4$. *Example: Scale III,* $\Omega_{0.26-0.81H} = 4.10-2.37$ (Fig. 7b). Scale III shows the opposite behaviour. It presents the same aspect and contraction ratios than Scale II, but a lower inlet area A_i that renders a higher inlet swirl intensity Ω_i. In contrast to Scales I and II, the flow reaches the top in Scale III at a much higher swirl intensity. Accordingly, the pressure rise originated in the contraction increases and its influence extends further (Escudier and Keller, 1985). Much higher velocities develop in Fig. 7b and a qualitative change is observed in the profiles. On the one hand, $\overline{U}_z$ shows a similar jet but with much larger values. On the other, the high swirl velocity at the bottom extends the region of solid body rotation beyond the area of influence of the contraction delimited by the diameter of the vortex finder $r \sim 0.30R$, which causes the reversion again. The recirculation zone generated acquires an annular shape between $0.30\,R < r < 0.65R$, that envelops the jet. At the top end, the recirculation zone has narrowed significantly but it is still maintained. Notice that the outer free like vortex starts immediately after the influence of the vortex finder at $r = 0.30\,R$, but in contrast to the observation in Scales I and II, it ceases at $r = 0.78R$ where $\overline{U}_\theta$ and $\overline{U}_z$ start a rapid decrease towards the wall.

4.1.3. Symmetry and distribution to the inlet nozzles

The design of the ring distributor and the feed from to the plenum (i.e. the ring that feeds the inlets in Fig. 1) can originate preferential paths in this sort of arrangements and result in asymmetrical flow fields (Huntington, 2004; Hreiz et al., 2011). In order to illustrate this phenomenon, the data in Scale III was collected using two types of distributors. Design 1 uses two separate branches both fed by the same inlet. Each feeds consecutive inlet ports at each side of the tower starting from the same location. The first pair that is fed constitutes neighbouring nozzles, and being the closest to the inlet, presents the lower pressure drop. The last pair, again neighbouring ports, is opposite to the inlet and the higher pressure drop is expected to result in lower air mass rates according to numerical simulations. In contrast, Design 2 uses an open bustle ring which is expected to aid balancing the pressure in all inlets and give comparable velocities in opposite ports (Huntington, 2004). Both systems are compared in Fig. 8. The use of the Design 1 results in larger differences in both sides, particularly in the recirculation zone $> 50\%$. In contrast, an open bustle ring reduces differences $< 10\%$., which confirms the optimal configuration and stresses the relevance of maintaining constant inlet velocities at all ports.

4.1.4. Self similarity

At sufficiently large *Re* numbers where viscous forces become less significant, or in fully rough regimes where drag is dependent on ε/D, the flow structure is expected to be self-similar. The data under cleaned walls confirmed such behaviour in a case where the contraction and Ω dominated the velocity profiles. It remains questionable in Cases B and C, where the vortex beaks down in the chamber. Fig. 9 compares the velocity field for *Re* in the range $10^5 - 2\cdot 10^5$ for Case C, showing that the shape of the vortex is maintained at high *Re* with independence of the *VBD* (confirmed up to $Re = 1.27\cdot 10^5$) However, as *Re* keeps on decreasing to Re_1, $\overline{U}_\theta$ becomes significantly lower and $\overline{U}_z$ diminishes at the top (see the transition from the outer to the inner regions at $z = 8.1D$). Such a phenomenon is indicative of a displacement in the position of the stagnation and suggests the loss of the self-similarity between $10^5 < Re < 1.27\cdot 10^5$.

4.1.5. The swirl decay

In a cleaned tower Ω_o reduces exponentially with *Re* independent decay rates, $\lambda \sim 0.08-0.09$ (Francia et al., 2015a), but the most relevant question is the impact of representative sets of deposits. The evolution of Ω_o under fouled walls is given in Fig. 10 and the fit to Eqs. (4) and (5) summarised in Table 3. The deposits clearly accelerate the decay. The axial rate of change of Ω_o in Fig. 10 (i.e. the effective wall shear stress) shows a clear relation to the location of the bands given in Table 2. Abrupt changes in Ω_o correlate to the location of the thickest bands within the spray

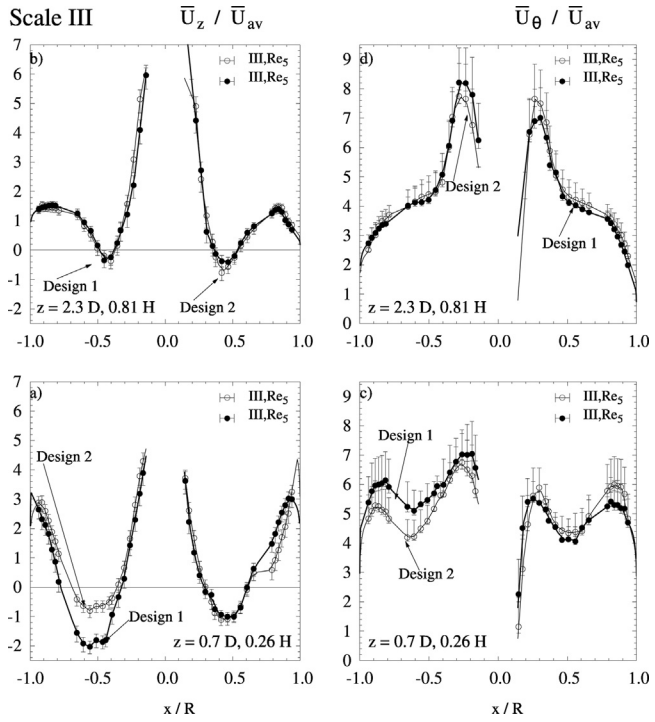

Fig. 8. Effect of the air distributor in vortex symmetry. Scale III. Design 1 (two branches) or Design 2 (an open bustle ring). (a,b) $\overline{U}_z$ (c,d) $\overline{U}_\theta$.

region and to the transitions between areas of patches and clean walls. At the bottom end the thickness is similar in Cases A and B, and in both Ω_o follows the same trend, λ rising up to 0.11 in B. However, reaching the spray region, in addition to the ε/D characteristic of the band, the flow is forced to overcome a step between patches of deposits onto homogeneous bands. In Case B a thick band appears between $5.7D < z < 7.1\,D$ (see Figs. 2 and 3), and causes a clear drop in Ω_o in Fig. 10. Note that this is unavoidable as a consequence of operating slurry nozzle(s). The same occurs in Case C, which commences with a higher initial Ω_o value at $z = 2.2\,D$ perhaps as the result of showing a clean cone (see Table 2). At the spray region between $3.3D < z < 7.1D$, the obstruction becomes much wider (see Figs. 2 and 3) and λ rises > 0.200. In both Cases B and C, Ω_o remains at stable values at the top end were there are no deposits.

A correlation between the angular momentum flow and the deposits coverage is a very relevant fact. Deposits appear not only responsible of the operation under a much weaker swirl, but crucially they are the origin of drastic changes in the structure. A rigorous numerical description remains an interesting challenge. It is unclear how obstructions such as those in Fig. 3 could be related to the roughness height ε/D used in available wall functions (e.g. Jimenez, 2004 or Volino et al., 2007). Yet reality dictates that deposits in dryers will be spatially distributed, shifting from regions of clean walls to uneven patches and stepping into bands of homogeneous thickness and ε/D. In some cases, they do not only disturb the boundary layer but are large enough to obstruct the convective flow. Clearly, this originates the initial drop in Ω_o for Case C, caused by the thick patch shown in Fig. 3 for $z < 3-4D$. The effect becomes clearer in the turbulent field described in Section 4.2.1.1 where the kinetic energy dissipated here from the convective flow is transferred into the turbulence.

The velocity profiles in Fig. 9 show a statistically significant difference, lost in the computation of λ (Re independent in Table 3 and Fig. 10) due to the extrapolation, the propagation of errors and the fit. According to the velocity field, one must expect that for $\Omega < 1$ the operation at $Re < 10^5$ is likely to increase λ. Such

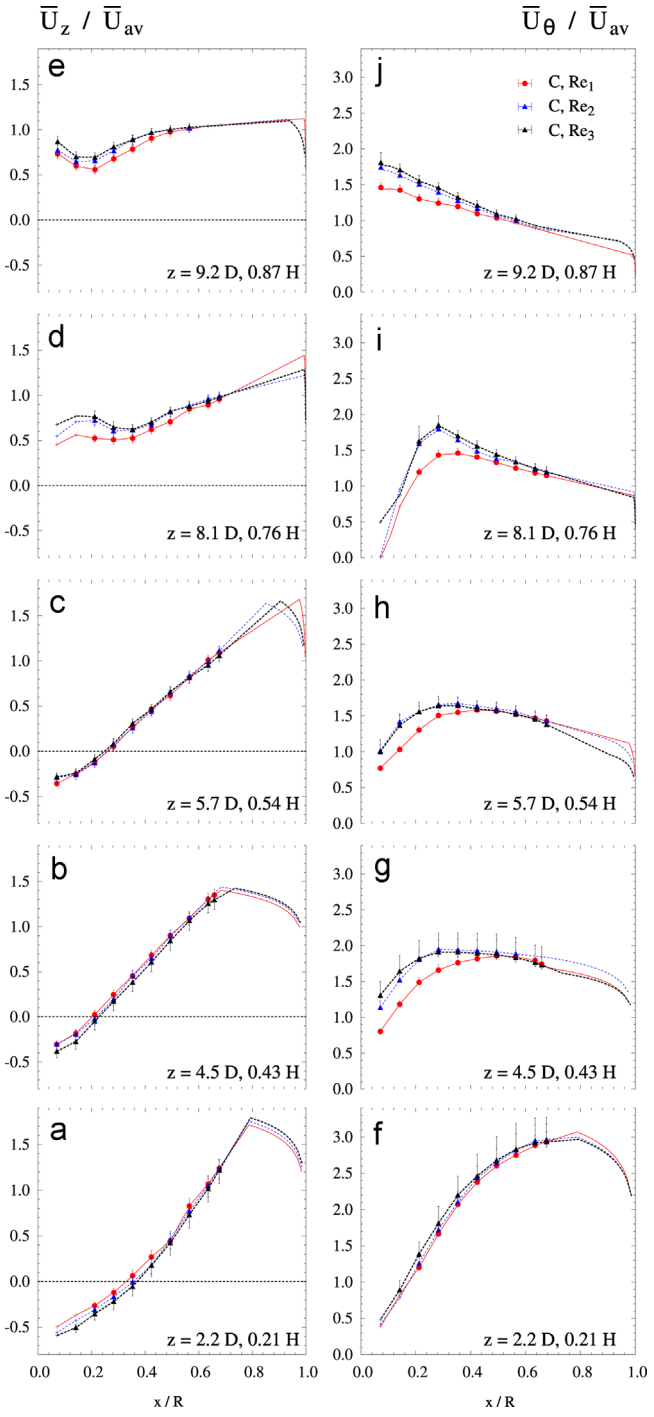

Fig. 9. Self similarity under heavy deposition. Case C, Scale I, across *Re*. Axial $\overline{U}_z$ (left) and tangential $\overline{U}_\theta$ (right) velocities for all levels.

behaviour appears only for Case C and not Case A, probably because the influence of the contraction decreases sufficiently for the flow to show the *Re* dependency of an open system.

Fig. 11 presents the evolution of Ω in Scales I, II, and III versus the axial position z normalised by the diameter D (Fig. 11a) or the length of the cylinder, H (Fig. 11b). The purpose is to compare positions at the same relative distance to the two low pressure points, at the exit duct and at the bottom core of the vortex. Scale II makes use a lower Ω_i but it also presents a shorter aspect ratio, H/D, which reduces the inner surface area. In this way, Scale II develops the same Ω than Scale I at the same relative distance to the exit in Fig. 11b. In combination with a similar contraction ratio,

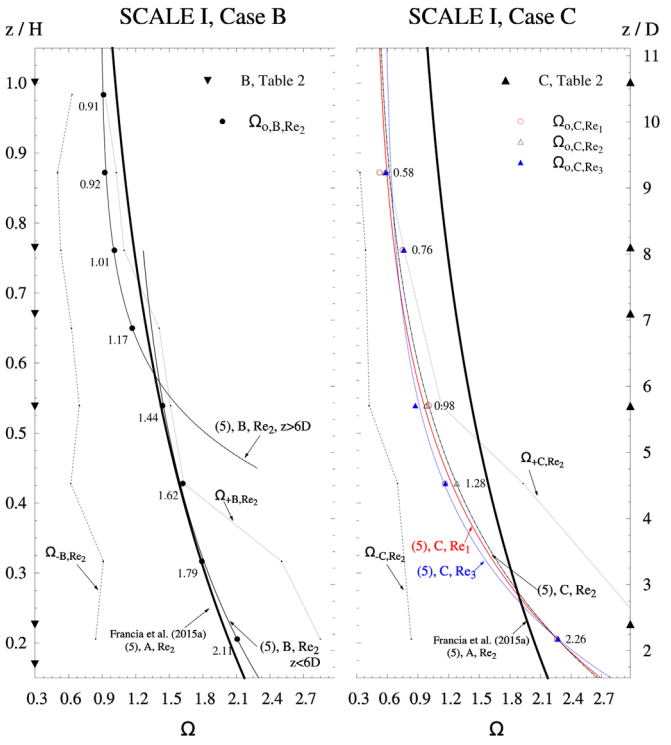

Fig. 10. Decay of Ω in the cylindrical chamber. Scale I under fouled walls. Standard and heavy deposition in Case B and Case C. The sections of deposits shown in Table 2 are highlighted in the y-axes. Ω_o, Ω_+ and Ω_- show the best estimate and over and under predictions; lines depict Eq. (5).

Table 3
Swirl decay rates under fouled walls. Fit to a proportional or linear relation between $\tau_{w,\theta}$ and Ω in Eqs. (4) and (5).

Case		$Re \cdot 10^{-5}$	Ω_r	A	B	λ
B	Re_2	1.44 ± 0.01	2.11	−0.075	0.026	0.114
$\boldsymbol{B_{z<6D}}$	Re_2	1.44 ± 0.01	2.11	−0.139	0.148	0.111
$\boldsymbol{B_{z>6D}}$	Re_2	1.44 ± 0.01	1.17	−0.379	0.336	0.085
C	Re_1	1.00 ± 0.01	2.26	−0.181	0.082	0.221
C	Re_2	1.55 ± 0.01	2.26	−0.165	0.073	0.211
C	Re_3	2.29 ± 0.02	2.27	−0.224	0.126	0.228

d/D, the acceleration caused by the exit duct has a similar influence and Scale I and II show comparable velocity profiles in respect to z/H in Fig. 7a, but not in respect to z/D. The mean velocity field can be scaled up but needs recognition of the effect of the swirl decay. In contrast, Scale III operates at a higher Ω_i and shows a significantly different velocity field. The decay rate, λ, increases up to ~ 0.200, which cannot be explained by the morphology of the deposits (i.e. evenly distributed in Scales II and III, see Fig. 3e). A higher λ is due to the change in the velocity direction near the wall, dominated by a high Ω and no longer comparable to an open system (e.g. Kitoh, 1991; Najafi et al., 2011). It appears that friction is function of Ω due the effect of the contraction, and Re independent at sufficiently large numbers.

4.1.6. *Strategies on the scale up of the fluid dynamics*

In scaling up complex flows, one expects the operation at the same Re (or sufficiently high) to render the same velocity field as long as geometrical similarity and scaled inlet conditions are maintained (Oakley, 1994). In the context of a tall-form dryer, the geometry is defined by the aspect H/D and contraction ratios

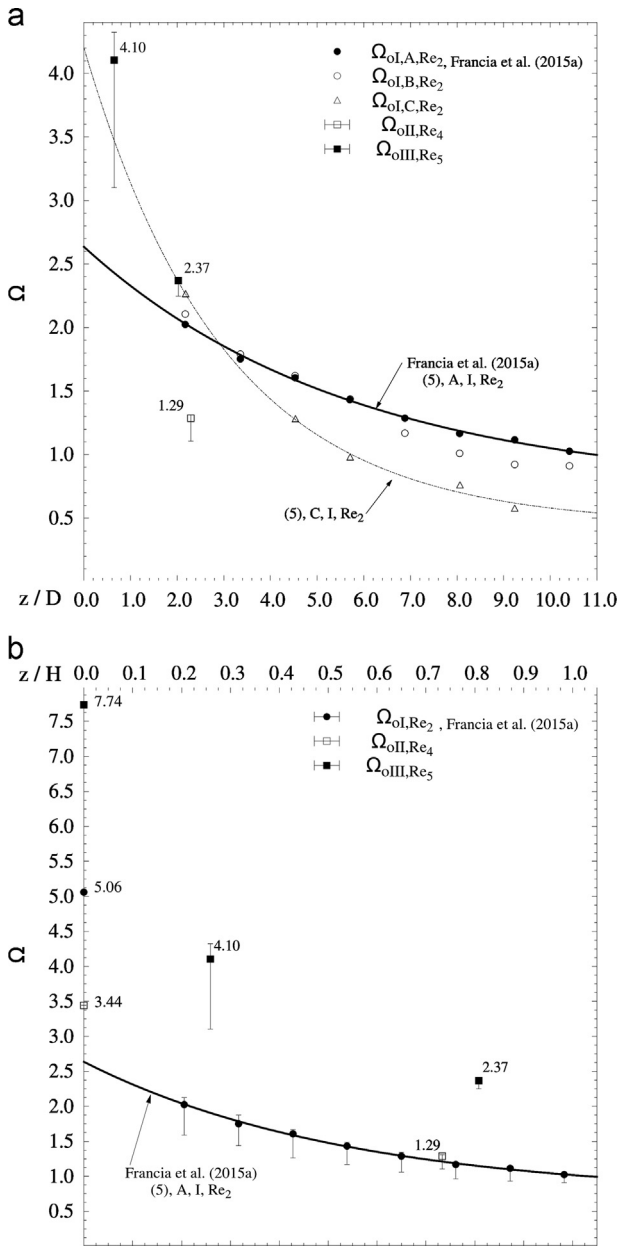

Fig. 11. Comparison of Ω_o and the decay rate λ across Scales I, II and III. Error bars indicate variation given by Ω_- and Ω_+, excluded in (a) for Scale I for clarity. Ω_i is plotted at $z=0$. (a) and (b) show respectively z/D or z/H. Data for Case A in (b) taken from Francia et al. (2015a).

d/D and the inlet conditions by the velocity profile that enters the cylinder. A similar dimensional analysis as those reported in cyclones (Zhao, 2010) can be undertaken but would lack the effect of gravity in the residence time of the solids. As described in Section 2.1, engineers tend to control residence time by the position of atomizers and the unit geometry, but then face a challenge in the changes of the centrifugal inertia and the flow patterns when the scale or the operating conditions vary.

Previous scale up analysis refer to the initial angular momentum of the flow or the geometry but do not consider the change in the wall shear stress due to the deposits. The effect of modifying Ω_i has become obvious in previous sections, but the successful transition from Scale I to Scale II demonstrates that it is possible to obtain a comparable flow structure if one maintains the evolution of Ω in the cylinder. The guidelines given by authors such as Masters (1995) or Kemp and Oakley (2002) needs to be

reconsidered in the context of swirl dryers to account for friction. In a given tower the swirl decay can be estimated making use of H/D, Eq. (5) and the decay rates reported in Table 3 for fouled walls. At first, the prediction can be used for design purposes and to determine the optimum tower R or R_i in new units, given that the length of the cylinder is likely limited by the desired particle residence time. Secondly, one can consider modifying Ω_i as a control tool. In a given tower R and R_i cannot be changed, but one can in principle modify Ω_i simply by constraining the combined area of the inlets A_i (i.e. having sufficiently powerful inlet fans) or modifying the operation of other swirl generation mechanisms (e.g. the use of vanes). In this way one can target a desired Ω range in the cylinder to drive or suppress the recirculation regions shown in Fig. 6. This philosophy can prove useful to accommodate changes in the process. For instance, currently it is impossible to control the attenuation of the swirl caused when the deposits grow in a changeover period (i.e. different formulations) or when loading rises at high production rates. All could be in principle accommodated by increasing Ω_i just in the adequate proportion to maintain a comparable Ω value at the top. Thirdly, manipulating the recirculation regions and the strength of the jet could be extremely powerful to control the elutriation rate and the particle residence time. In this sense, the use of computational fluid dynamics models may be able to optimise the location and alignment of nozzles, but it is vital that current models gain the ability to predict the swirl decay and the recirculation revealed here.

4.2. Turbulence statistics

4.2.1. Turbulent kinetic energy and normal stresses

4.2.1.1. Production of turbulence owed to friction. Fig. 12 shows the axial development of the turbulent kinetic energy κ and normal stresses under fouled walls, and compares the maximum values obtained to the range observed in a cleaned tower. κ is known to reach high values in the inner region, due the instability of the core, and a maximum in the outer region that shifts inwards close to the top exit (Francia et al., 2015a). In spite of the uncertainty, it is obvious that deposits in Cases B and C modify both, the value and the profile of κ. Standard deposit bands in Case B make κ to rise $\sim$67 % from a maximum value in the outer region of 0.09 $\overline{U}_{av}^2$ to 0.15 $\overline{U}_{av}^2$. In this case κ does not show a clear outer maximum, but remains constant in the cross section. It decreases axially until reaching the *VBD* position between $z = 5.7\,D$ and $6.9\,D$ where it rises again to similar values than in the operation with cleaned walls. Case C follows a very similar pattern. The deposits are much wider at the bottom and this makes κ in the outer region to increase even further, to 0.17 $\overline{U}_{av}^2$, after which it shows the same axial evolution: a sustained decrease towards the top, in this case to slightly lower values, 0.01 $\overline{U}_{av}^2$.

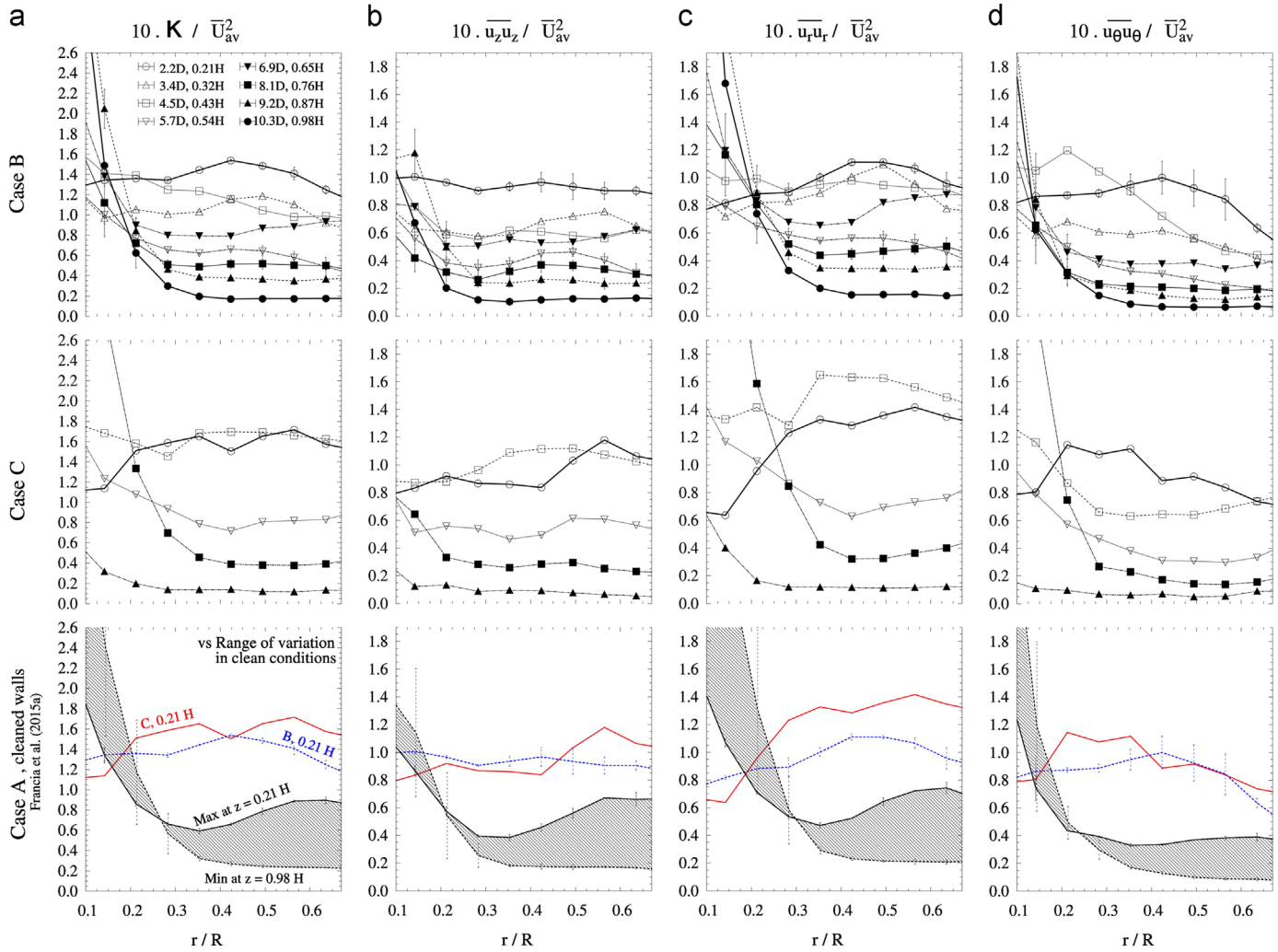

Fig. 12. The impact of deposits in turbulence. Scale I. (a) κ (b) $\overline{u_z u_z}$, (c) $\overline{u_r u_r}$, (d) $\overline{u_\theta u_\theta}$. The shaded range for cleaned walls, Case A is adapted from Francia et al. (2015a). Error bars indicate variation across tangential locations. Maximum measurement uncertainty in κ is -7, $+31$ %, in $\overline{u_z u_z}$ -41, $+19$%, in $\overline{u_r u_r}$ -35, $+22$% and in $\overline{u_\theta u_\theta}$ -23, $+19$% (Francia, 2015).

For the most part, the axial decrease of κ can be explained by the relation between κ and Ω, instrumental to heat and mass transfer processes (Chang and Dhir, 1994, 1995). The presence of deposits enhances the drag and originates a substantial transfer of kinetic energy from the convective flow (i.e. observed as a decay in Ω) into the turbulence, provided on the one hand by the drag against larger roughness elements and in the other by the *VBD*. Case C is a clear example. Friction is mainly originated by a large patch of deposits in the spray region (i.e. notice the distribution of patches in Figs. 2 and 3 for $z<3-4D$). Despite the drastic drop in Ω in Fig. 10, the generation of turbulence maintains κ constant below $z\leq 5.7D$. After this point, the deposits are reduced and one observes how Ω_o drops from 0.98 to 0.58 in Fig. 10 and κ decays in Fig. 12a. As a passing note, this behaviour suggests potential for applying similar rough surfaces with the objective of generating turbulence at the cost of swirl intensity in systems where deposition may not be an issue, as for instance the improvement of local mixing in reactive swirling flows.

Under fouled walls, $\overline{u_z u_z}$ shows a flat radial profile and losses the maxima characteristic of a cleaned tower. In turn, $\overline{u_r u_r}$ in Fig. 12c remains constant at the bottom of the dryer and decreases only at the core in Case C. All normal stresses show a similar axial axial development in Cases B and C: they decrease until the breakdown location, after which there is an increase and then a final decay close the exit. It can appreciated how in Case B the outer maxima in $\overline{u_z u_z}$ and $\overline{u_r u_r}$ are disrupted near the breakdown, $5.7D<z<6.9D$ and recover after it. Under fouled walls all normal stresses show comparable values below the *VBD*, but in a cleaned tower $\overline{u_\theta u_\theta}$ is known to have lower values and a flat profile (Francia et al., 2015a). The different behaviour observed under stronger friction is in good agreement with our previous assertion in Francia et al. (2015a), which on the basis of the study of Derksen (2005) attributed the suppression of $\overline{u_\theta u_\theta}$ to the influence of the contraction, limited in Cases B and C.

4.2.1.2. Relation to Re and Ω range. Both larger towers show higher κ values in Fig. 13. Interestingly, Scales I and II present a similar κ range and comparable profiles in Fig. 13a but in this case in terms of z/D, which points to the difficulty in scaling up both the mean flow and the turbulent field with a different aspect ratio. In addition, Scale II shows a larger maximum in the annular region and it can be noted how $\overline{u_\theta u_\theta}$ and $\overline{u_z u_z}$ rise near wall where measurements are not available in Scale I. The increase in κ is emphasised moving to Scale III in Fig. 13b, which exhibit values up to ten times higher and a different radial profile. At the bottom a central maximum is associated to the jet and contained within the diameter of the vortex finder. In the annular part, κ and all the normal stresses increase towards the wall. At the top of the unit $\overline{u_r u_r}$ and $\overline{u_z u_z}$ show respective maxima beyond $r>0.30R$, which are likely associated to the abrupt decay in $\overline{U}_\theta$ and linked to the outer free vortex.

4.2.2. Reynolds stresses

Fig. 14 includes the structure of Reynolds stresses under fouled walls and different scales. Similarly to the reports in a cleaned tower, $\overline{u_z u_\theta}$ is predominately positive for Cases B and C in Fig. 14a and shows maximum values in the outer region that shift inwards until the flow reaches the *VBD*. After this point it moves outwards again and decreases substantially in value. Despite the large increase in κ associated to the friction, $\overline{u_z u_\theta}$ is only significantly higher at the bottom. In Case B, $\overline{u_z u_\theta}$ takes predominately negative values at the core, as in the case of cleaned walls, but in Case C positive values occur also at the centre. $\overline{u_r u_\theta}$ shows a different axial development. While in a cleaned tower only positive values occur, in Cases B and C, $\overline{u_r u_\theta}$ turns negative at the bottom and

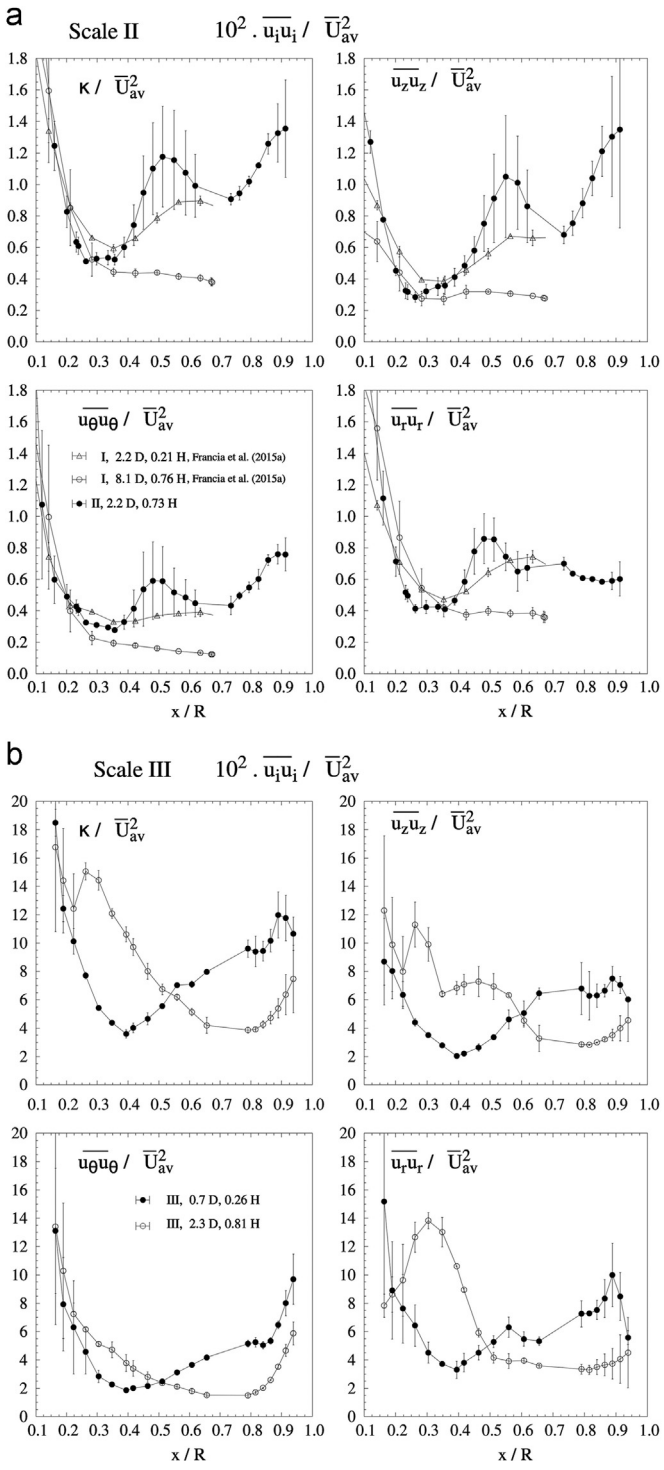

Fig. 13. Turbulence across scales. (a) Scale II, (b) Scale III. Scale II is compared to data for Case A taken from Francia et al. (2015a). Error bars indicate variation across tangential locations. For uncertainty see Fig. 12.

undergoes a rapid change in direction between $2.2D<z<3.4D$ and again to negative values at the core for $z>3.4D$. Under the presence of deposits, the negative values observed for $\overline{u_r u_z}$ at the outer part of the vortex are substantially higher under fouled walls.

Fig. 14 includes Scales II and III. Interestingly, all Reynolds stresses for both towers increase in then near wall region. In Scale II, $\overline{u_r u_\theta}$ shows a distinct maximum in the outer part, beyond the point of minimum axial velocity ($r\sim 0.45R$), which is absent in Scale I. In contrast, Scale III exhibits Reynolds stresses ten times

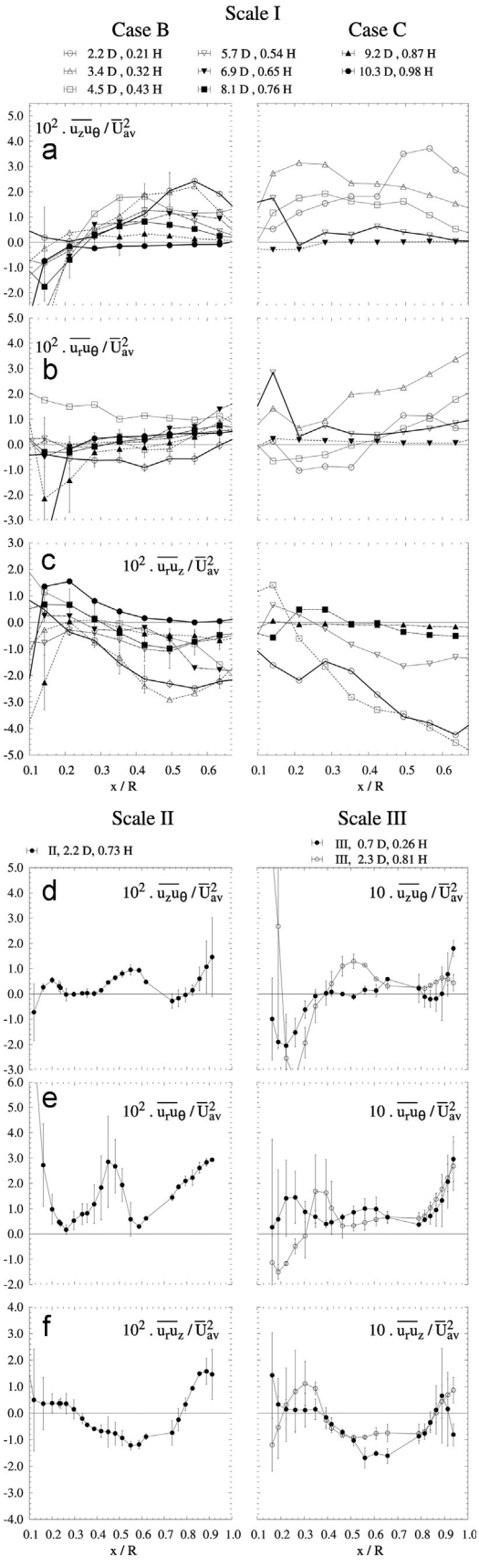

Fig. 14. Reynolds stresses. (a–d) $\overline{u_z u_\theta}$; (b–e) $\overline{u_r u_\theta}$; (c–f) $\overline{u_r u_z}$. Error bars indicate variation across tangential locations. Maximum measurement uncertainty in $\overline{u_z u_\theta}$ is ± 60 % in $\overline{u_r u_\theta}$ ± 100% and in $\overline{u_r u_z}$ $\pm 200-400$% (Francia 2015).

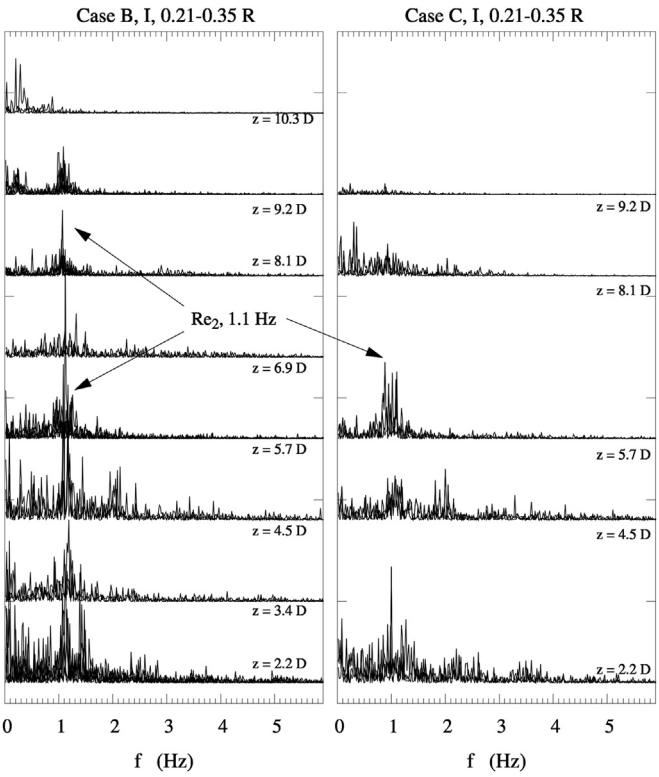

Fig. 15. Periodical structures. Periodogram of U in Scale I. $0.21R < r < 0.35R$. From left to right, Case B and C, at Re_2 in Table 2. Arbitrary y units.

higher. Despite the uncertainty, $\overline{u_r u_z}$ and $\overline{u_r u_\theta}$ show similar profiles and $\overline{u_z u_\theta}$ develops a maximum positive values in the outer region and a transition to negative in the jet, but in this case they turn positive again in the core as opposed to Scales I and II.

4.2.3. *Periodical phenomena*

The precession of the vortex core and the presence of large amplitude oscillations are well documented in cyclones and reported by many authors in dryers, such as Usui et al. (1985), Kieviet et al. (1997) or Southwell and Langrish (2001). The use of anemometry permitted the study of the same phenomena in reproducible conditions for a cleaned tower (Francia et al., 2015a). In this work, Scales II and III show similar large time scale oscillations in the top part of the jet, in the order of $0.2-0.3$ Hz but no higher frequencies. Interestingly, the flow in Scale I under fouled walls maintains the same higher frequency oscillations observed in Case A. Fig. 15 shows the time scales contained in the velocity signal by superimposing the periodograms obtained from a Fast Fourier Transform (*FFT*). Higher frequency oscillations appear in Cases B and C at all the levels below the *VBD*, and remarkably, comparison at different *Re* numbers in Case C confirms that the precession occurs at the same Strouhal number *St* reported for cleaned walls $St \approx 1.4-1.5$ (Francia et al., 2015a).

5. Conclusions

This work details the response of the air fluid dynamics in counter-current swirl dryers to the actual range of Ω and walls deposits observed in the manufacture of detergents. The following general conclusions can be summarised:

a) *Wall friction:* It has been investigated in manufacturing swirl dryers using typical uniform bands of deposits and heavily built up walls with thick patches. The deposits cause a clear increase in friction versus the observations with smooth walls or in cleaned towers with rough walls. The friction causes a substantial increase of the turbulence kinetic energy, κ, and the rate of decay of the swirl, λ, from 0.08 to 0.20 as a function of the coverage and the deposits thickness, and independently of Re for $Re > 1.27.10^5$. The inclusion of wall deposits in the perdition of swirl decay, design criteria and the development of models is of paramount importance as otherwise over-prediction of velocities between $40-186\%$ must be expected.

b) *Recirculation:* The changes in Ω destabilise the flow and lead to the formation of areas of reverse flow, or recirculation. A transition between three different flow regimes appears (1) central recirculation, (2) no recirculation and (3) annular recirculation operating at constant exit contraction ratio, $d/D \sim 0.30$. In systems where a low Ω prevails at the top, $\Omega_e < \sim 1$ the vortex breaks down within the cylindrical chamber and creates a central recirculation zone, *CRZ*, at the bottom, of larger extension and strength for decreasing Ω_e. When the swirl intensity rises to $\Omega_e > \sim 1$, the acceleration caused by the contraction suppresses the *VBD* and the *CRZ* and a central jet is form across the unit. A further increase to $\Omega_e > \sim 2.4$ causes another substantial rise in velocities. In this case, the recirculation region extends beyond the influence of the vortex finder and takes an annular shape that envelops the jet. The transition shows that is not possible to predict the flow field in a counter-current swirl dryer on the basis of geometry alone. One needs also to consider the swirl decay across the chamber. Scale up and control strategies have been proposed based in controlling inlet swirl intensity to manipulate the flow regime by usage of the inlet parameters, correlations and rates reported here.

c) *Turbulence:* The turbulent kinetic energy, κ, and all normal stresses are in the one hand correlated to Ω, and in the other respond to the friction. Wall deposits modify both, the values and the evolution across the chamber. Typical deposits thickness and coverage increases κ up to $67-88$ % versus the use of cleaned walls. The distribution of Reynolds stresses follows different flow structures, what may serve as a guide to assess the performance of closure models. Interestingly, the higher frequencies oscillations, indicative of the precession of the vortex core occur at a constant *St* number in towers with high aspect ratios, independently on Ω and the vortex breakdown but are lost in the shorter units.

Nomenclature

A	swirl decay rate in Eq. (5)
A_c	cross sectional area in the cylinder, m^2
A_i	combined area of all inlet nozzles, m^2
B	swirl decay constant in Eq. (5)
D	diameter of the cylinder, m
G_θ	axial angular momentum flux, kg m^{-1} s^{-2}
$G_{z,av}$	average axial momentum flux, kg s^{-2}
$\overline{M}_c$	mass rate through the cylinder, kg s^{-1}
$\overline{M}_i$	combined mass rate through the inlets, kg s^{-1}
H	distance from air inlets to vortex finder, m
R	radius of the cylinder, m
R_i	radius of the cross-section at the inlets, m
Re	Reynolds number $Re = DU_{av}/\nu$
$\overline{U}$	time averaged air velocity / component, m s^{-1}
$\overline{U}_{av}$	bulk or superficial velocity $\overline{U}_{av} = \overline{M}_C/\rho A_C$, m s^{-1}
$\overline{U}_i$	velocity at the inlets $\overline{U}_i = \overline{M}_i/\rho A_i$, m s^{-1}
St	Strouhal number $St = f \cdot D/\overline{U}_{av}$
d	diameter of the vortex finder, m
f	oscillation frequency, Hz
r	coordinate in the radial direction, m
u	velocity fluctuation, m s^{-1}
x	distance from the wall along the orthogonal, m
z	axial position, m

Greek letters

Ω	swirl intensity
α	anemometer misalignment over a_2 in Fig. 1c, rad
β	anemometer misalignment over a_3 in Fig. 1c, rad
ε	roughness height, m
ξ	axial alignment of the air inlet nozzles. rad
γ	anemometer misalignment over a_1 in Fig. 1c, rad
λ	swirl decay rate in Eq. (4)
κ	specific turbulent kinetic energy, m^2 s^2
ρ	density, kg m^{-3}
τ	shear stress, kg m^{-1} s^{-2}
υ	kinematic viscosity/Eddy viscosity, m^2 s^{-1}
φ	radial alignment of the air inlet nozzles, rad

Subscripts, superscripts and caps

A, *B*, C	Cases A, B or C showing different wall deposits.
I, II, III	for Scales I, II and III defined in Table 1.
r, z, θ	along radial, vertical and tangential direction.
$^\circ$, $-$, $+$	best estimate, under and over estimation.
ref	a reference height, or length, in Eqs. (4) and (5).
w	at the wall.

Abbreviations

CRZ	central recirculation region.
PVC	precession of the vortex core.
VBD	vortex breakdown.

Acknowledgements

VF was supported by an Engineering Doctorate Studentship sponsored by the Engineering and Physical Sciences Research Council (EPSRC) grant number EP/G036713/1, and Procter & Gamble in the Industrial Doctoral Centre in Formulation Engineering, School of Chemical Engineering, University of Birmingham.

References

Ali, M., 2014. Numerical Modelling of a Counter-Current Spray Drying Tower. University of Leeds (Ph.D. thesis).

Avci, A., Irfan Karagoz, I., Surmen, A., 2013. Development of a new method for evaluating vortex length in reversed flow cyclone separators. Powder Technol. 235, 460–466.

Bayly, A. E., Jukes, P., Groombridge, M., McNally, C., 2004. Airflow patterns in a counter-current spray drying tower – simulation and measurement. International Drying Symposium, Sao Paulo, 22–25 B, pp. 775–781.

Butner, H., 1999. Dimensionless representation of particle separation characteristic of cyclones. J. Aerosol Sci. 30 (10), 1291–1302.

Chang, F., Dhir, V.K., 1994. Turbulent flow field in tangentially injected swirl flows in tubes. Int. J. Heat Fluid Flow 15 (5), 346–356.

Chang, F., Dhir, V.K., 1995. Mechanisms of heat transfer enhancement and sloe decay of swirl in tubes using tangential injection. Int. J. Heat Fluid Flow 16 (2), 78–87.

Chen, J., Shi, M., 2007. A universal model to calculate cyclone pressure drop. Powder Technol. 171, 184–191.

Cortes, C., Gil, A., 2007. Modeling the gas and particle flow inside cyclone separators. Prog. Energy Combust. Sci. 33, 409–452.

Derksen, J.J., 2005. Simulations of confined turbulent vortex flow. Comput. Fluids 34, 301–318.
Derksen, J.J., Van den Akker, H.E.A., 2000. Simulation of vortex core precession in a reverse-flow cyclone. AIChE J. 46 (7), 1317–1331.
Escudier, M.P., Bornstein, J., Zehnder, N., 1980. Observations and LDA measurements of confined turbulent vortex flow. J. Fluid Mech. 98 (1), 49–63.
Escudier, M.P., Keller, J.J., 1985. Recirculation in swirling flow: a manifestation of vortex breakdown. AIAA J. 23 (1), 111–116.
Francia, V., 2015. Spray Drying of Detergents in Counter-Current Towers: A Study of Turbulent Swirling Flows, Fouling and Agglomeration. University of Birmingham, Birmingham, UK (EngD thesis).
Francia, V., Martin, L., Bayly, A.E., Simmons, M.J.H., 2015a. An experimental investigation of the swirling flow in a tall-form a counter-current spray dryer. Exp. Therm. Fluid Sci. 65, 52–64.
Francia, V., Martin, L., Bayly, A.E., Simmons, M.J.H., 2015b. The role of wall deposition and re-entrainment in swirl spray dryers. AIChE J. 61 (6), 1804–1821.
Francia, V., Martin, L., Bayly, A.E., Simmons, M.J.H.,2015c. Use of sonic anemometry for the study of turbulent air swirling flows in large confined industrial units. Submitted for publication.
Harvie, D.J.E, Langrish, T.A.G., Fletcher, D.F., 2001. Numerical simulations of the gas flow patterns within a tall form spray dryer. Trans IChemE 79, 235–248.
Hassall, G., 2011. Wall Build Up in Spray Driers. Chemical Engineering. University of Birmingham, Birmingham. UK (EngD thesis).
Hoekstra, A.J., Derksen, J.J., Van Den Akker, H.D.A., 1999. An experimental and numerical study of turbulent swirling flow in gas cyclones. Chem. Eng. Sci. 54, 2055–2065.
Hoffmann, A.C, Santen, A.V, Allen, R.W.K., Clift, R., 1992. Effects of geometry and solid loading on the performance of gas cyclones. Powder Technol. 70, 83–91.
Hoffmann, A.C., de Jonge, R., Arends, H., Hanrats, C., 1995. Evidence of the 'natural vortex length' and its effect on the separation efficiency of gas cyclones 32, 799–804Filtr. Sep. 32, 799–804.
Hreiz, R., Gentric, C., Midoux, N., 2011. Numerical investigation of swirling flow in cylindrical cyclones. Chem. Eng. Res. Des. 89, 2521–2539.
Huntington, D.H., 2004. The influence of the spray drying process on product properties. Dry. Technol. 22 (6), 1261–1287.
Jimenez, J., 2004. Turbulent flow over rough walls. Annu. Rev. Fluid Mech. 36, 173–196.
Kaya, F., Karagoz, I., Avci, A., 2011. Effects of surface roughness on the performance of tangential inlet cyclone separators. Aerosol Sci. Technol. 45, 988–995.
Kim, C.H, Lee, J.W., 2001. A new collection efficiency model for small cyclones considering the boundary-layer effect. J. Aerosol Sci. 32, 251–269.
Kemp, I.C., Oakley, D.E., 2002. Modeling of particulate drying in theory and practice. Dry. Technol. 20 (9), 1699–1750.
Kieviet, F.G., Van Raaij, J., De Moor, P.P.E.A, Kerkhof, P.J.A.M., 2001. Measurement and modelling of the air flow pattern in a pilot-plant spray dryer. Trans IChemE 75A, 312–328.
Kitoh, O., 1991. Experimental study of turbulent swirling flow in a straight pipe. J. Fluid Mech. 225, 445–479.
Langrish, T.A.G, Williams, J., Fletcher, D.F., 2004. Simulation of the effects of the inlet swirl on gas flow patterns in a pilot-scale spray drier. Chem. Eng. Res. Des. 82, 821–833.
Liu, Z., Jiao, J., Zheng, Y., Zhang, Q., Jia, L., 2006. Investigation of turbulence characteristics in a gas cyclone by stereoscopic PIV. AIChE J. 52 (12), 4150–4160.
Luca-Negro, O., O'Doherty, T., 2001. Vortex breakdown: a review. Prog. Energy Combust. Sci. 27, 431–481.
Masters, K., 1995. Scale-up of spray dryers. Dry. Technol. 12 (1–2), 235–257.
Najafi, A.F., Mousavian, S.M., Amini, K., 2011. Numerical investigations on swirl intensity decay rate for turbulent swirling flow in a fixed pipe. Int. J. Mech. Sci. 53, 801–811.
Oakley, D.E., 1994. Scale-up of spray dryers with the air of computational fluid dynamics. Dry. Technol.: Int. J. 12 (1–2), 217–233.
Oakley, D.E., 2004. Spray dryer modeling in theory and practice. Dry. Technol.: Int. J. 22 (6), 1371–1402.
Paris, J.R., Ross, P.N., Dastur, S.P., Morris, R.L., 1971. Modeling of the air flow pattern in a counter current spray-drying tower. Ind. Eng. Chem. Process Des. Dev. 10, 2.
Paiva, J., Romualdo Salcedo, R., Araujo, P., 2010. Impact of particle agglomeration in cyclones. Chem. Eng. J. 162, 861–876.
Peng, W., Hoffmann, A.C., Dries, H.W.E, Regelink, M.A., Stein, L.E., 2005. Experimental study of the vortex end in centrifugal separators: the nature of the vortex end. Chem. Eng. Sci. 60, 6919–6928.
Pisarev, G.I, Hoffmann, A.C., Peng, W., Dijkstra, H.A., 2011. Large Eddy simulation of the vortex end in reverse-flow centrifugal separators. Appl. Math. Comput. 217, 5016–5022.
Pisarev, G.I, Gjerde, V, Balakin, B.V, Hoffmann, A.C., Dijkstra, H.A., Peng, W., 2012. Experimental and computational study of the "end of the vortex" phenomenon in reverse-flow centrifugal separators. AIChE J. 58 (5), 1371–1380.
Senoo, Y, Nagata, T, 1972. Swirl flow in long pipes with different roughness. Bull. JSME 5 (90), 1514.
Sharma, S., 1990. Spray Dryer Simulation and Air Flow Pattern Studies. The University of Aston, Birmingham. UK (Ph.D. thesis).
Sloan, D.G., Smisth, P.J., Smooth, L.D., 1986. Modeling of swirl in turbulent flow systems. Prog. Energy Combust. Sci. 12, 163–250.
Southwell, D.B., Langrish, T.A.G., 2001. The effect of the swirl on the stability of spray dryers. Trans I Chem E 79, 222–234.
Steenbergen, W., Voskamp, J., 1998. The rate of decay of swirl in turbulent pipe flow. Flow Meas. Instrum. 9, 67–78.
Syred, N., 2006. A review of oscillation mechanisms and the role of the precessing vortex core (PVC) in swirl combustion systems. Prog. Energy Combust. Sci. 32, 93–161.
Usui, H., Sano, Y., Yanagimoto, Y., Yamasaki, Y., 1985. Turbulent flow in a spray drying chamber. J. Chem. Eng. Jpn. 18, 3.
Verdurmen, R.E.M., Menn, P., Ritzert, J., Blei, S., Nhumaio, G.C.S., Sørensen, T.S., Gunsing, M., Straatsma, J., Verschueren, M., Sibeijn, M., Schulte, G., Fritsching, U., Bauckhage, K., Tropea, C., Sommerfeld, M., Watkins, A.P., Yule, A.J., Schønfeldt, H., 2004. Simulation of agglomeration in spray drying installations: the EDECAD project. Dry. Technol. 22 (6), 1403–1461.
Volino, R.J., Schultz, M.P., Flack, K.A., 2007. Turbulence structure in rough–and smooth-wall boundary layers. J. Fluid Mech. 592, 263–293.
Wawrzyniak, P., Podyma, M., Zbicinski, I., Bartczak, Z., Rabaeva, J., 2012. Modeling of air flow in an industrial counter-current spray drying tower. Dry. Technol. 30, 217–224.
Weber, R, Dugué, J., 1992. Combustion accelerated swirling flows in high confinements. Prog. Energy Combust. Sci. 18, 349–367.
Zbicinski, I., Piatkowski, M., 2009. Continuous and discrete phase behavior in counter current spray drying. Dry. Technol. 27 (12), 1353–1362.
Zhao, B., 2010. Development of a Dimensionless Logistic Model for Predicting Cyclone Separation Efficiency. Aerosol Sci. Technol. 44 (12), 1105–1112.